Bioactive Materials 21 (2023) 129–141

Contents lists available at ScienceDirect

Bioactive Materials

journal homepage: www.keaipublishing.com/en/journals/bioactive-materials

Cobalt protoporphyrin-induced nano-self-assembly for CT imaging, magnetic-guidance, and antioxidative protection of stem cells in pulmonary fibrosis treatment

Yimeng Shu [a,b], Ming Ma [a,b,c,**], Xiaoxia Pan [d], Muhammad Shafiq [e], Huizhu Yu [a,b], Hangrong Chen [a,b,c,*]

[a] State Key Laboratory of High Performance Ceramics and Superfine Microstructures Shanghai Institute of Ceramics, Chinese Academy of Sciences, Shanghai, 200050, PR China
[b] Center of Materials Science and Optoelectronics Engineering, University of Chinese Academy of Sciences, Beijing, 100049, PR China
[c] School of Chemistry and Materials Science, Hangzhou Institute for Advanced Study, University of Chinese Academy of Sciences, 1 Sub-lane, Xiangshan, Hangzhou, 310024, PR China
[d] State Key Laboratory of Molecular Engineering of Polymers, Department of Macromolecular Science, Fudan University, Shanghai, 200438, PR China
[e] Department of Biotechnology, Faculty of Science and Technology, University of Central Punjab (UCP), Lahore, 54000, Pakistan

ARTICLE INFO

Keywords:
Self-assembly
Pulmonary fibrosis
Cell labeling
Stem cell therapy
Theranostic

ABSTRACT

Mesenchymal stem cells (MSCs) transplantation is a promising approach for pulmonary fibrosis (PF), however it is impeded by several persistent challenges, including the lack of long-term tracking, low retention, and poor survival of MSCs, as well as the low labeling efficiency of nanoprobes. Herein, a cobalt protoporphyrin IX (CoPP) aggregation-induced strategy is applied to develop a multifunctional nano-self-assembly (ASCP) by combining gold nanoparticle (AuNPs), superparamagnetic iron oxide nanoparticles (SPIONs), and CoPP through a facile solvent evaporation-driven approach. Since no additional carrier materials are employed during the synthesis, high loading efficiency of active ingredients and excellent biocompatibility are achieved. Additionally, facile modification of the ASCPs with bicyclo[6.1.0]nonyne (BCN) groups (named as ASCP-BCN) enables them to effectively label MSCs through bioorthogonal chemistry. The obtained ASCP-BCN could not only help to track MSCs with AuNP-based computed tomography (CT) imaging, but also achieve an SPIONs-assisted magnetic field based improvement in the MSCs retention in lungs as well as promoted the survival of MSCs *via* the sustained release of CoPP. The *in vivo* results demonstrated that the labeled MSCs improved the lung functions and alleviated the fibrosis symptoms in a bleomycin–induced PF mouse model. Collectively, a novel ASCP-BCN multifunctional nanoagent was developed to bioorthogonally-label MSCs with a high efficiency, presenting a promising potential in the high-efficient MSC therapy for PF.

1. Introduction

Pulmonary fibrosis (PF), as a chronic and fatal interstitial lung disease characterized by the progressive lung scarring and interstitial pneumonia, usually leads to a significant decrease in the lung function [1]. The median survival time of PF is only 3–5 years, which is even shorter than that of common cancers [2,3]. Although different types of clinical treatments, such as chemotherapy and oxygen therapy have been leveraged to impede or even reversing the progression of the PF, their therapeutic outcomes are still unsatisfactory, which necessitate the development of new and effective therapies [4,5].

In the past decade, mesenchymal stem cells (MSCs) have received considerable attention for the PF management, by alleviating the PF *via* multiple mechanisms, including cell differentiation, paracrine factors

Peer review under responsibility of KeAi Communications Co., Ltd.
* Corresponding author. State Key Laboratory of High Performance Ceramics and Superfine Microstructures Shanghai Institute of Ceramics, Chinese Academy of Sciences, Shanghai, 200050, PR China.
** Corresponding author. State Key Laboratory of High Performance Ceramics and Superfine Microstructures Shanghai Institute of Ceramics, Chinese Academy of Sciences, Shanghai, 200050, PR China.
E-mail addresses: mma@mail.sic.ac.cn (M. Ma), hrchen@mail.sic.ac.cn (H. Chen).

https://doi.org/10.1016/j.bioactmat.2022.08.008
Received 30 March 2022; Received in revised form 9 August 2022; Accepted 9 August 2022

secretion, mitochondria transfer, and resolution of the lung inflammation by macrophages polarization [5]. Nonetheless, so far only a few clinical trials on stem cell treatment of PF have been carried out around the world, which showed limited therapeutic effects [6,7]. The low retention and poor survival rate of the administered MSCs in the fibrotic lungs are the main reasons for their poor clinical translation [8]. While the narrow lung capillaries initially retain MSCs after intratracheal or intravenous administration, most of the exogenous MSCs are drained off from the lungs within first 24 h [8,9]. Moreover, the excessive amount of the reactive oxygen species (ROS) in lungs of PF patients seriously limit the survival of transplanted MSCs [10]. These limitations impede the lungs to maintain enough living MSCs, thereby halting a sustained and an effective anti-fibrosis effect [11]. In parallel, the assessment of stem cell tracking and their bio-distribution is pivotal to ascertain the safety and therapeutic efficacy of MSC therapy [12]. While a number of imaging modalities based on contrast agents, such as computed tomography (CT), magnetic resonance imaging (MRI) and ultrasound imaging (USI) have been developed for real-time stem cell tracking, they still face several limitations, including poor imaging contrast and sensitivity of the labeling agents, low cell labeling efficiency, and extensive *in vitro* manipulations of cells, *etc* [13,14]. Thus, development of a multi-modal strategy that may offer a solution to the above-mentioned issues in stem cell-based PF therapy is highly desired [3].

Recently, theranostic nanomaterials have garnered significant interests of the research community for stem cell engineering owning to their illustrious potentials for the simultaneous imaging and payload release [15]. For example, Jokerst et al. incorporated insulin-like growth factors (IGFs) and superparamagnetic iron oxide nanoparticles (SPIONs) into large-pore silica nanoparticles-based carriers to integrate dual-modal ultrasound/magnetic resonance (US/MR) imaging and cell survival promotion functions into a single labeling nanoagent [16]. Lu et al. also exploited SPIONs as MRI tracer of stem cells; the SPIONs were coated with cationic polymersome to transfect siRNA for inducing the neuronal differentiation of the exogenous stem cells [17]. Similarly, Qi et al. developed Wnt3a (Wnt Family Member 3A)-loaded porous silicon nanoparticles with both ultrasound imaging and antioxidative cytoprotection functions to label stem cells for enhancing their therapeutic effect [18]. Besides, Wang et al. integrated fluorescent silver sulphide (Ag_2S) quantum dot, retinoic acid, and a SOX9 siRNA-expressing plasmid porphyrin poly(beta-amino esters) into poly(D, L-lactide-co-glycolide) (PLGA) carriers to simultaneously achieve real-time fluorescence tracking and neural differentiation of the labeled stem cells [19]. While these theranostic labeling nanoagents may improve the efficacy of stem cell therapy by solving different clinical issues, their translation is still hindered because of an imperfect utility of each nanoagnet type, as well as high complexity and poor reproducibility in materials synthesis. Additionally, host-carriers (i.e., silica and PLGA) with lack of therapeutic or imaging capabilities occupy major weight ratio of the nanoparticles, which result in a significant increase in the effective dose of the entire labeling nanoagent used for stem cell labeling, thereby inducing potential toxicity and immunogenic responses to the patients [20]. Consequently, development of an "all-in-one" labeling nanoagent with simple synthetic approach and high content of active ingredients is highly required but has not been realized yet.

Metalloporphyrins are an important class of metal organic compounds with numerous biological functions, which emanate from their central metal atoms [21,22]. As one of the representative metalloporphyrin derivative, cobalt protoporphyrin IX (CoPP) has been proven to effectively upregulate the expression of cytoprotective protein heme oxygenase-1 (HO-1) in various types of cells (*e.g.* dendritic cells, cardiomyocytes, stem cells, etc.), which can increase their resistance against oxidative stress, and may attenuate different types of diseases, such as myocardial infarction, ischemic stroke and organ fibrosis [23,24]. However, exposure to the excessive amount of CoPP may impart toxicity to stem cells, which necessitates design of a sustained release system to maintain an appropriate concentration of the CoPP in stem cells [25,26].

Herein, a CoPP aggregation-induced nano-self-assembly, named as AuNPs/SPIONs@CoPP nanoagent (ASCP), was constructed by a simple solvent evaporation-driven method (shown in scheme 1a) for MSCs labeling, wherein CoPP serves as an HO-1 inducer, while AuNPs and SPIONs endow ASCP with the functions of enhanced CT imaging and magnetic manipulation, respectively. It is worth mentioning that no additional components other than CoPP, SPIONs, and AuNPs were used during the synthesis of ASCP, ensuring a high payload of cytoprotective drugs and functional nanoparticles, and thereby reducing the dose of the exogenous agents required for MSC labeling. Moreover, the exposed carboxyl groups on the particle surface of ASCP, conferred by the CoPP not only render water solubility to ASCP, but also enable its further functionalization *via* a simple amide coupling reaction. Based on these distinct advantages, the linkers composed of amino groups, polyethylene glycol (PEG) chains and bicyclo[6.1.0]nonyne (BCN) were conjugated onto ASCPs (named ASCP-BCN here) to achieve a quick, high-efficiency, and safe labeling of MSCs *via* a cooper-free biorthogonal chemistry. Owing to the good magnetism of the labeled MSCs endowed by SPIONs, the retention of MSCs implanted in lungs could be significantly increased by the manipulation of the external magnetic field. Meanwhile, the AuNPs inside ASCP may allow us to track and quantify MSCs *in vivo* through CT imaging. More importantly, the sustained intracellular release of the CoPP from ASCP-BCNs could enhance the ability of MSCs to resist oxidative stress for a long period of time, thereby prolonging their survival time after transplantation. Taking the advantages offered by ASCP-BCNs, they can be regarded as a potential "all-in-one" labeling nanoagent for MSCs-based PF therapy (Scheme 1b). The effects of ASCP-BCN labeled MSCs on the lung function recovery and the degree of lung fibrosis were systemically evaluated in a bleomycin-induced PF model to confirm the prospect of this nano-self-assembly in MSC-based therapy.

2. Results and discussion

2.1. Synthesis and characterizations of ASCP-BCN

In order to provide enhanced CT imaging and magnetic functions for the labeling agent, firstly, monodispersed 1-dodecanethiol-modified AuNPs and oleic acid-modified SPIONs were prepared by biphasic reduction and thermal decomposition, respectively (the morphologic characterization is shown in Fig. S1). The synthesized AuNPs and SPIONs were next mixed with CoPP at an appropriate proportion in an organic solvent and sonicated in water to form a homogeneous oil-in-water microemulsion. Considering the hydrophobic surface of AuNPs and SPIONs, we expected that they may self-assemble with CoPP through *via* intermolecular hydrophobic-hydrophobic interaction [27]. The spherical hydrophilic ASCP nanoagents were then obtained by removing organic solvent through evaporation followed by dialysis. Subsequently, BCN-PEG_3-NH_2 was chemically conjugated to the ASCP by a simple EDC/NHS-mediated amidation reaction.

Transmission electron microscopy (TEM) images of ASCP-BCN revealed that multiple NPs and CoPP self-assembled into spherical particles with an uneven internal structure (Fig. 1a). Interestingly, the high angle annular dark-field (HAADF) TEM images and element mapping images confirmed that AuNPs tended to aggregate on only one side of the particles, while SPIONs and CoPP distributed randomly (Fig. 1b). The formation of such a unique structure can be explained by the asymmetric contraction of AuNPs during evaporation [28,29]. The lattice fringes corresponding to the (111) lattice planes of AuNPs and (220) lattice planes of SPIONs can be identified in the high resolution TEM (HRTEM) images (Fig. 1c), and the corresponding diffraction ring can be found in select-area electron diffraction (SAED) patterns. Similarly, the main diffraction peaks of X-ray diffraction (XRD) at 38° and 35° corresponded to the (111) lattice planes of AuNP and (311) lattice planes of

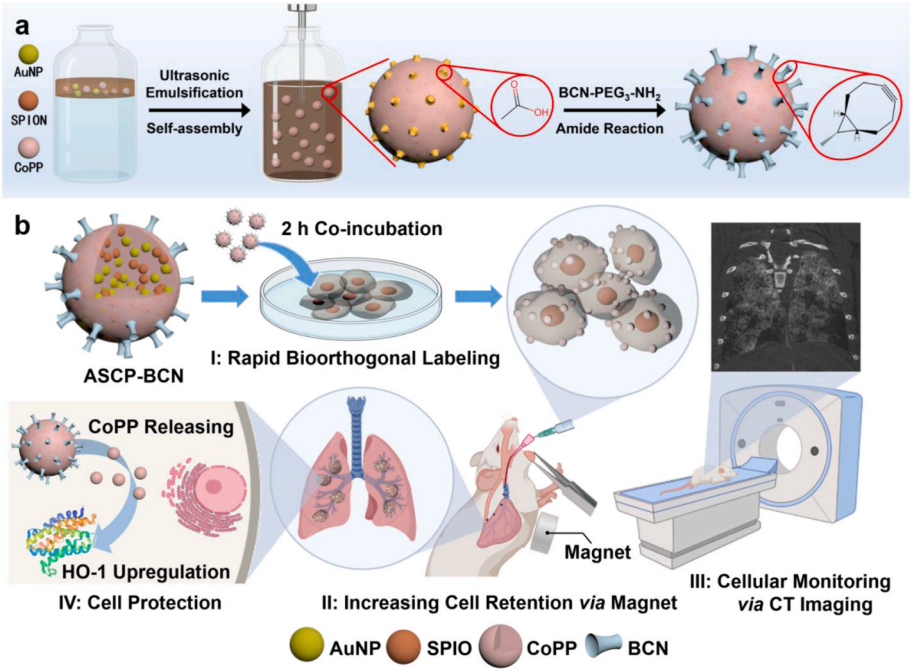

Scheme 1. (a) Schematic illustration of the synthesis of ASCP-BCN. (b) Schematic illustrating of the quadruple function of ASCP-BCN for PF therapy: (I) labeling MSCs with high efficiency and safety *via* a cooper-free biorthogonal reaction, (II) increasing retention of transplanted MSCs in lungs *via* magnets, (III) *in vivo* monitoring the transplanted MSCs *via* CT imaging, and (IV) protecting transplanted MSCs against oxidative stress in the oxidative microenvironment of fibrotic lungs.

SPIONs, respectively (Fig. S2). Altogether, these results demonstrated that the crystalline structure of the AuNPs and SPIONs could be well maintained during the nano-self-assembly process.

The successful modification of ASCP with BCN was ascertained by the characteristic peaks of alkynyl groups in the ^{1}H NMR spectra of ASCP-BCN (Fig. 1d). Moreover, the surface charge of ASCP significantly increased from −28 eV to −15 eV after BCN modification (Fig. 1e). This can be attributed to the substitution of the carboxyl groups (−COOH) of ASCP by the BCN-PEG$_3$-NH$_2$ through amide linkages. Furthermore, we dissolved ASCP and ASCP-BCN in PBS at the same concentration and added azidosilane by maintaining the temperature at 37 °C for 1 h to simulate the bioorthogonal labeling process. As shown in Fig. S3, the silicon-to-gold ratio was much higher in ASCP-BCN group than that of the ASCP group, which also confirmed the successful modification of BCN.

ASCP-BCNs also displayed a Tyndall effect, thereby demonstrating their good dispersity in deionized water (Fig. S4). The average hydrodynamic particle size of ASCP-BCN in water was arround 123 nm, which could remain stable in either water or PBS for up to 14 days, or in culture medium for up to 5 days, confirming the good stability of these particles (Fig. 1f, g and Fig. S5). As shown in Fig. S6, the high resolution X-ray photoelectron spectroscopy (XPS) spectra of Co2p exhibited two peaks at 796.0 eV (2p3/2) and 780.6 eV (2p1/2), which are the typical characteristics peaks of Co(II) in CoPP [30]. Besides, the weight percentage of CoPP in ASCP-BCN was 27.6% as calculated by inductively coupled plasma mass spectroscopy (ICP-MS). Intriguingly, the absorption peak of free CoPP at 421 nm was red-shifted to 427 nm after the formation of ASCP-BCN, thereby indicating a self-assembly of CoPP through π-π stacking interactions (Fig. S7) [31]. Furthermore, the CoPP release behavior in different environments was investigated by dialysis method, where the ASCP-BCNs were immersed in PBS at pH 4.5 or pH 7.4 containing 100 μM hydrogen peroxide (H_2O_2) to simulate the acidic microenvironment of lysosome as well as the inflammatory microenvironment of the lungs during PF, respectively. The CoPP showed similar sustained release curves under different circumstances, and the accumulative release of CoPP under the normal condition (pH = 7.4), acidic condition (pH = 4.5) and simulated oxidative stress condition (pH = 7.4 with H_2O_2) was calculated to be 21.0%, 21.1% and 18.5% in the first 3 days (Fig. 1h). To further ascertain whether the sustained release would cause the degradation of the nano-self-assembly, the morphology of ASCP-BCNs after 5 days of dialysis was characterized through TEM. It was found that the SPIONs and AuNPs well remained in the particles without disintegration after dialysis in normal, acidic, or simulated oxidative stress environments (Fig. S8), indicative of good stability of the obtained ASCP-BCNs.

Thereafter, the magnetic and imaging functions of ASCP-BCN were evaluated. To dissect the influence of different components on the magnetic properties of particles, a reference nanoagent (named as CPSP) synthesized by self-assembling only SPIONs and CoPP was used as a control group. The magnetization curves of SPIONs, CPSP, and ASCP-BCN at room temperature demonstrated their superparamagnetic characteristics, which exhibited the saturation magnetization (σ_s) values of 32.2, 46.0, and 37.4 emu/g of Fe_3O_4, respectively (Fig. 1i). The higher value of σ_s for CPSP and ASCP-BCN is ascribed to the less spin disordered surfaces of these nanoagents; the CPSP exhibited relatively higher σ_s owing to the higher content of Fe_3O_4 in this nanoagents.

As a powerful CT contrast agent, AuNPs exhibit 2.7 times higher x-ray attenuation per mass as compared to the iodine, which is a clinical CT contrast agent, enabling effective tracing of MSCs *in vivo* at a relatively low and safe dose [32]. The X-ray attenuation property of ASCP-BCN was evaluated by acquiring CT images of the synthesized nanoagents at different gradient concentrations. The ASCP-BCN nanoagents gradually generated brighter CT signals with an increase in the Au content, where the quantitative result manifested linear relationship between the Hounsfield unit (HU) of ASCP-BCN and the Au concentration ($R^2 = 0.99$). The slope was calculated to be 1.43, demonstrating an enhanced CT imaging function of such nano-self-assembly (Fig. 1j and k).

2.2. Bioorthogonal labeling and CT imaging of MSCs

So far, conventional methods of stem cell labeling based on an active or passive intracellular delivery of nanoparticles have been performed, which require a 24 h co-incubation and are time-consuming and less

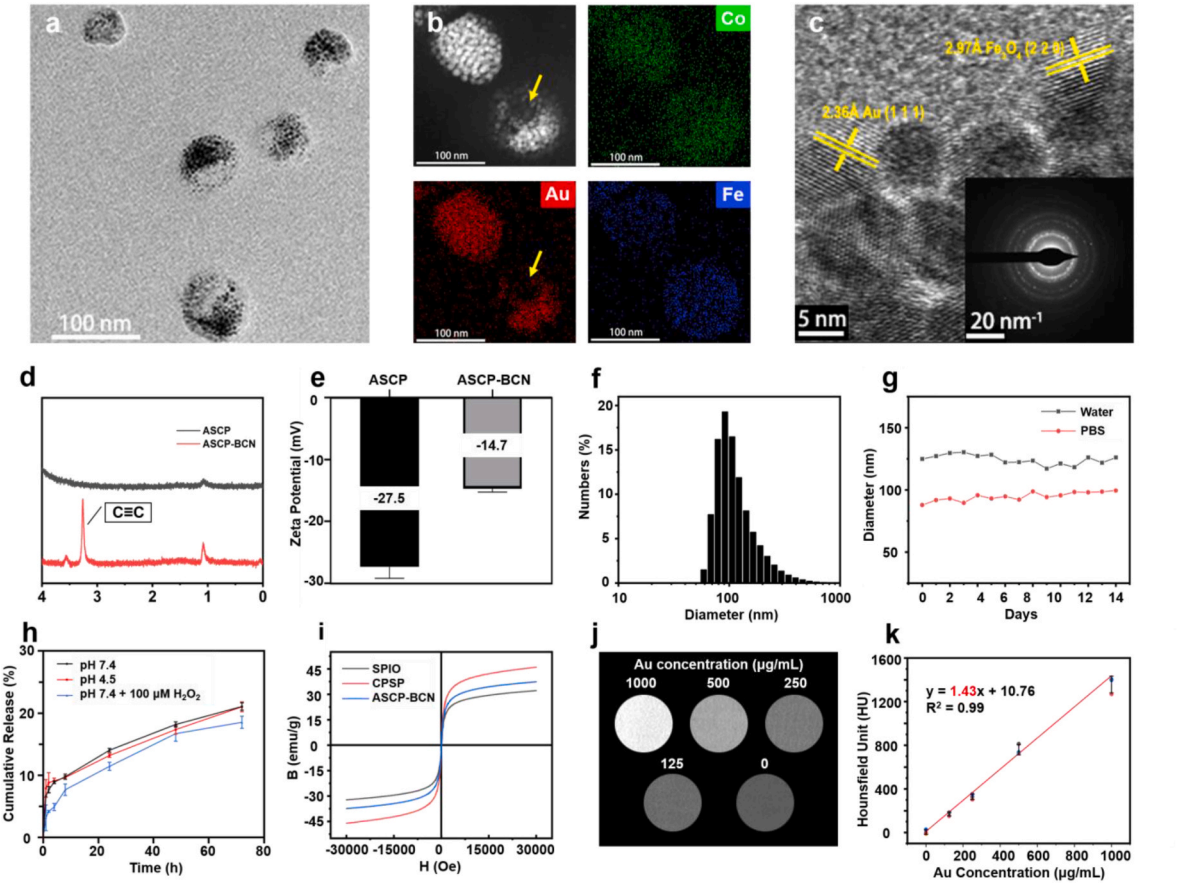

Fig. 1. Characterizations of ASCP-BCN. (a) TEM image of ASCP-BCN. (b) High-angle annular dark field image and element mappings of ASCP-BCN. The yellow arrow indicates the part without AuNPs (c) HRTEM image and selected area electron diffraction pattern of ASCP-BCN. (d) ^{1}H NMR spectra of ASCP and ASCP-BCN. (e) Zeta potentials of ASCP and ASCP-BCN. (f) Hydrodynamic size distribution of ASCP-BCN. (g) Hydrodynamic diameter of ASCP-BCN in water and PBS for up to 14 days. (h) Cumulative release curves of CoPP from ASCP-BCN after immersion in PBS at pH 7.4 in the absence or presence of H_2O_2, as well as PBS at pH 4.5. (i) Magnetic hysteresis loops of SPION, CPSP, and ASCP-BCN. (j) CT images of ASCP-BCN aqueous solutions at different concentrations. (k) Calculated HU values of ASCP-BCN aqueous solutions at diverse concentrations of Au.

efficient [33,34]. Despite the development of various methods for an efficient labeling of stem cells with nanoagents, such as cationic polymer modification, they still suffer from the potential side effects of hindering stem cell proliferation and differentiation [13]. In order to improve the MSC labeling efficiency of the nanoagent, meanwhile to ensure good biocompatibility, a bioorthogonal strategy was harnessed in this work (Fig. 2a). We firstly produced the targetable exogenous chemical receptors on the surface of MSCs by a 48 h pretreatment with 10 μM Ac_4ManNAz, which is a metabolic precursor containing azide groups. Thereafter, ASCP-BCN (40 μg/mL) were co-incubated with MSCs (about 2×10^5 cells per well) for 2 h. The exact position of ASCP-BCNs on the MSCs was characterized by SEM. As anticipated, the unlabeled MSCs exhibited a sleek surface, while bioorthogonally labeled MSCs displayed numerous ASCP-BCN nanoagents all over their surface, suggestive of the existence of an effective ligation between the ASCP-BCNs and the azide groups on the MSCs (Fig. 2b and c). The cross-sectional images of ASCP-BCN labeled MSCs were acquired by TEM to further validate the distribution and the stability of nanoagents in MSCs. As shown in Fig. 2d, nanoagents were found both on the MSC surface and in the cytoplasm just after labeling. Besides, a number of ASCP-BCNs with intact structure could still be observed in the lysosomes and the cytoplasm of the MSC at day 2 after labeling with ASCP-BCN, implying good stability of the ASCP-BCN even in the acidic environment of the lysosomes (Fig. S9). Furthermore, Prussian blue (PB) staining for iron assessment was conducted to compare the amount of labeling nanoagents in MSCs *via* different labeling approaches (Fig. 2e). MSCs labeled with the ASCP-BCN showed a large quantity of the blue-colored nanoagents. In contrast, the MSCs which were not pretreated with Ac_4ManNAz, or ASCP which was not functionalized with the BCN showed significantly less content of blue-colored nanoagents. According to the ICP-MS data, BCN modification could increase the labeling efficiency of the nanoagent from 48% to 73% (Fig. 2f). More specifically, the average amounts of CoPP, AuNPs, and SPIONs in each labeled MSC were about 8.1×10^{-5} μg, 1.1×10^{-4} μg, and 1.0×10^{-4} μg, respectively. These results indicate that metabolically engineered MSCs could be efficiently labeled by ASCP-BCN *via* copper-free bioorthogonal click chemistry.

The potential of ASCP-BCN-labeling for CT tracing of MSCs was evaluated *in vitro*. In detail, after pretreatment with Ac_4ManNAz, MSCs were co-incubated with ASCP-BCNs at different concentrations (0, 10, 20, and 40 μg/mL) for 2 h separately. The labeled MSCs were collected to observe CT phantom images. As compared to the unlabeled MSCs, the labeled MSCs exhibited significantly stronger CT signal. Besides, the HU values of labeled MSCs and the concentration of the added ASCP-BCN coincided with an imperfect linear relationship (the coefficient of determination was calculated to be 0.96; Fig. 2g and Fig. S10). This result indicates that the labeling efficiency of MSCs was slightly different when they were co-cultured with the different concentrations of ASCP-BCN. However, for MSCs labeled with a specific concentration of nanoagent (*e.g.*, 40 μg/mL), the CT signal of labeled MSCs increased linearly with the increase in the number of MSC, showing a high coefficient of determination of 0.99 (Fig. 2h and Fig. S10). Furthermore, the labeling stability of the ASCP-BCNs on the MSCs was evaluated through

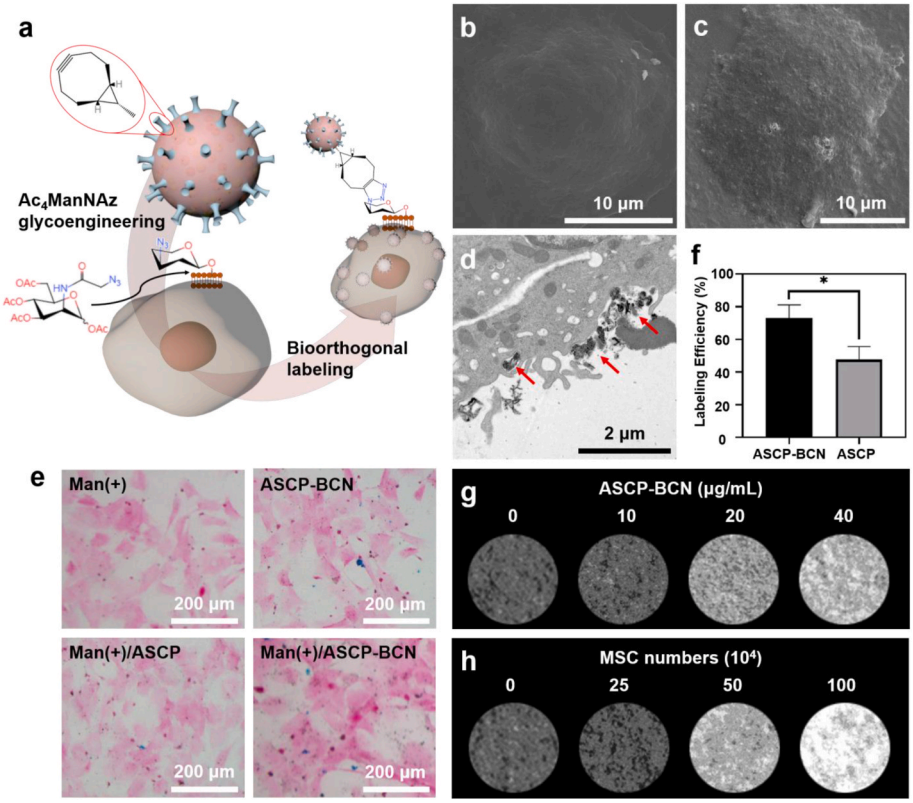

Fig. 2. *In vitro* bioorthogonal labeling of MSCs with ASCP-BCN (a) Schematic illustration of the MSC labeling method by metabolic glycoengineering and copper-free click bioorthogonal reaction. (b, c) SEM images of the (b) unlabeled and (c) labeled MSCs. Scale bar, 10 μm. (d) TEM images of labeled MSCs. The red arrows indicate the ASCP-BCNs adhering to the surface of the MSC or endocytosed by the MSC. (e) Prussian blue staining of MSCs treated with $Ac_4ManNAz$, ASCP-BCN, $Ac_4ManNAz$/ASCP, and $Ac_4ManNAz$/ASCP-BCN. (f) Labeling efficiency of ASCP-BCN and ASCP content evaluated by ICP-OES, (*) $p < 0.05$. (g) *In vitro* CT images of PBS solutions containing 5×10^5 MSCs labeled by ASCP-BCN at different concentrations and (h) different amount of MSCs labeled by 40 μg/mL ASCP-BCN.

ICP-OES and CT imaging. As compared to the day 0 (just after labeling), the labeling efficiency of the ASCP-BCNs on the MSCs at day 7 still remained for up to 78%, indicative of good labeling stability, *i.e.,* most of the ASCP-BCNs kept labeling on the MSCs (Fig. S11). Besides, though the CT signal of the ASCP-BCNs labeled MSCs at day 7 was slightly lower than that of the labeled MSCs at day 0, the CT signal was still significant and satisfactory (Fig. S12). These results prove good labeling stability of the ASCP-BCN, which may offer a promising prospect for the quantitative CT tracking of MSCs for transplantation.

2.3. Effects of ASCP-BCN labeling on cell viability, differentiation, and migration

To assess the feasibility of bioorthogonal-labeling of MSCs with ASCP-BCN, the viability and multipotent differentiation of the labeled MSCs was evaluated. The viability of MSCs after incubation with different concentrations of ASCP-BCN ranging from 0 to 80 μg/mL for 1, 7, and 14 days was measured with the CCK-8 assay. The viability of labeled MSCs did not appreciably change for up to 80 μM ASCP-BCN even after 14 days of co-incubation (Fig. 3a). Furthermore, the MSCs treated with 40 or 80 μg/mL of ASCP-BCN for day 1 were stained with calcein-AM/propidium iodide (PI) kit, where the live and dead MSCs emitted green and red fluorescence, respectively. As shown in Fig. 3b, almost all of the labeled MSCs displayed green fluorescence, and no significant differences in proportion of live/dead cells were observed.

MSCs are pluripotent cells with the ability to differentiate into various cell lineages. To verify whether the pluripotency of MSCs would be affected by the $Ac_4ManNAz$ glycoengineering and the ASCP-BCN biorthogonal labeling, we performed osteogenic or adipogenic differentiation of labeled or unlabeled MSCs. For osteogenic differentiation, different types of the cells, such as untreated MSCs, $Ac_4ManNAz$ pretreated MSCs, and ASCP-BCN labeled MSCs showed an intense staining for alizarin red S, which is ascribed to the calcium nodules produced by MSCs (Fig. 3c). In addition, untreated and treated MSCs did not appreciably differ in terms of the content of calcium nodules (Fig. 3d). Similarly, MSCs in the control as well as three experimental groups exhibited the formation of lipid droplet after adipogenic induction for up to day 14; the amount of the generated lipid droplets showed an insignificant difference among various groups (Fig. 3c, e). These results established that the bioorthogonal labeling of MSCs with ASCP-BCN negligibly affected their differentiation potential.

It is reported that MSCs can migrate to the injury sites in response to the injury signals, which is an important mechanism for MSC-based therapy. Consequently, we assessed the migration of unlabeled as well as bioorthogonally-labeled MSCs *in vitro*, which showed an insignificant difference in the migratory potential of MSCs in both groups, further indicating the feasibility of ASCP-BCNs for MSC therapy (Fig. S13).

2.4. Antioxidant stress effect of ASCP-BCN

The low cell viability after transplantation has been impeding the development of MSC based therapy for PF, which is mainly because of the inflammatory environment and excessive oxidative stress in the lungs of PF patients [8]. Fortunately, CoPP has been reported to improve the resistance of transplanted MSCs against oxidative stress and improve their survival through activating the ERK/NRF2 signal pathway and increasing the expression levels of HO-1 [35]. To confirm whether the CoPP in the ASCP-BCN nano-self-assembly can still retain its antioxidative effect, the expression levels of HO-1 of the labeled MSCs under oxidative stress were evaluated *via* western blotting. As expected, the expression of HO-1 was upregulated by the H_2O_2 oxidative stress. It was further revealed that the labeling of MSCs with ASCP-BCN could significantly upregulate their expression level of HO-1, indicative of a higher resistance to the oxidative stress (Fig. 4a and b). To gain a further insight, the viability of MSCs labeled with the different concentrations of ASCP-BCNs was evaluated after 24 h of co-incubation in serum-free low-glucose medium containing 100 μM H_2O_2, thus mimicking an excessive oxidative stress microenvironment in the lungs of PF patients.

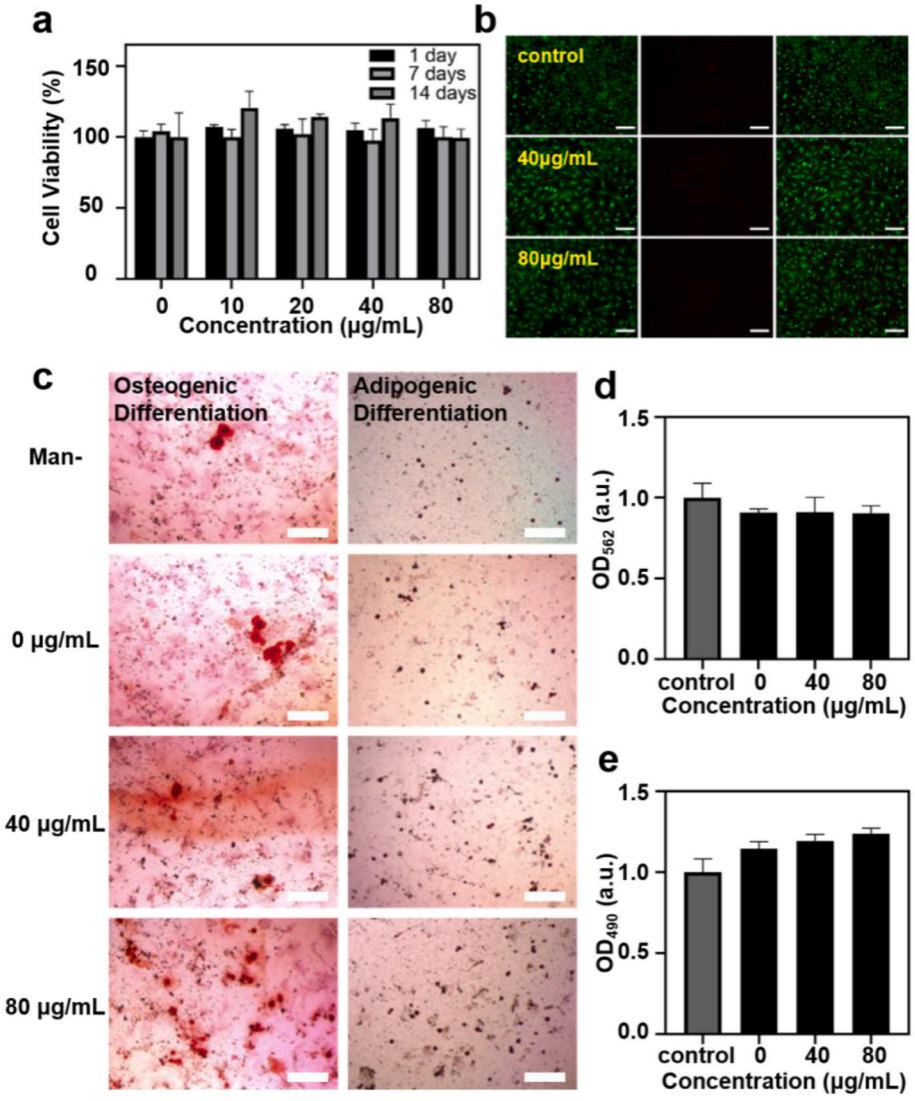

Fig. 3. Effect of ASCP-BCN biorthogonal labeling on the viability and pluripotency of MSCs. (a) Relative cell viability of MSCs labeled with different concentrations of ASCP-BCNs at day 1, 7and 14. (b) Fluorescence microscopy images of calcein-AM/PI stained MSCs after co-incubation with ASCP-BCNs at different concentrations at day 1. Scale bar, 100 μm. (c) Osteogenesis and adipogenesis of MSCs without any treatment (control) and with different treatments (Ac_4ManNAz glycolengineering alone or bioorthogonal labeling with 40 and 80 μg/mL of ASCP-BCNs) were observed by Alizarin Red S staining, and oil red O staining. Scale bar, 200 μm. (d) Absorbance values of dissolved calcium deposits at 562 nm in MSCs at day 14 of osteogenesis induction. (e) Absorbance values of dissolved lipid droplets at 490 nm in MSCs at day 14 after adipogenesis induction.

The labeled MSCs conferred a dose-dependent improvement in the cell survival once the ASCP-BCN concentrations were varied from 10 through 40 μg/mL (Fig. 4c). Specifically, the survival rate of MSCs labeled with 40 μg/mL of ASCP-BCN was increased by 19.2% than that of their unlabeled counterparts. Notably, the viability of the MSCs labeled with 80 μg/mL of ASCP-BCN showed some decrease as compared to the cells which were labeled with 40 μg/mL of ASCP-BCN. The compromised protective effect of the ASCP-BCN at the high concentration may be ascribed to enhanced oxidative damage induced by the excessive increase in HO-1 [36]. Moreover, ASCP-BCN labeling reduced cell apoptosis as revealed by using calcein-AM/PI staining. As shown in Fig. S14, a few MSCs displayed red PI fluorescence due to the cell apoptosis in H_2O_2-induced oxidant stress group, while the apoptosis rate was significantly decreased by the labeling of ASCP-BCN. Overall, these results indicate antioxidantive potential of ASCP-BCN, ensuring its protection function for MSC-based PF treatment.

2.5. Magnetic guided retention of MSCs in vitro

While superparamagnetic ASCP-BCN with high σ_s could be manipulated by an external magnetic field, it remains yet to be explored whether MSCs labeled by ASCP-BCNs could respond to an external magnetic field. Consequently, both unlabeled and labeled MSCs were seeded in a 24-well cell culture plate equipped with a pair of NdFeB magnets under each well for up to 24 h. By Giemsa staining, it was revealed that the labeled MSCs tended to be settled down in the magnetic pole regions, while unlabeled MSCs settled randomly (Fig. 4d–f). This magnetic-guided cell settling was further ascertained by incorporating a rubidium magnet to the suspension of the labeled MSCs (Fig. S15). Moreover, a plastic cylinder tube was applied to better mimic the environment of transplanted MSCs *in vivo*. The labeled MSCs suspension was injected into the tube at a flow rate of 0.2 mL/min, which were initially washed away with the suspension in the absence of a magnet (Fig. 4g). By contrast, the labeled MSCs were found to be accumulated on the wall of the tube once they were exposed to a magnet, further validating the successful magnetization of MSCs by ASCP-BCN.

2.6. Biosafety of ASCP-BCN and biodistribution of ASCP-BCN transplanted with MSCs

Prior to the *in vivo* evaluation, the biocompatibility of ASCP-BCN was assessed to confirm its feasibility for MSC-based therapy. A total 15 male BALB/c mice were randomly divided into 3 groups (n = 5) and were intravenously injected with the different doses of ASCP-BCN (*e.g.*, 0, 10, and 20 mg/kg, *etc.*). The mice were sacrificed at day 30 after injection. The blood as well as major organs (*e.g.*, heart, liver, spleen, lung, and kidney, *etc.*) were collected for a systematic assessment. The

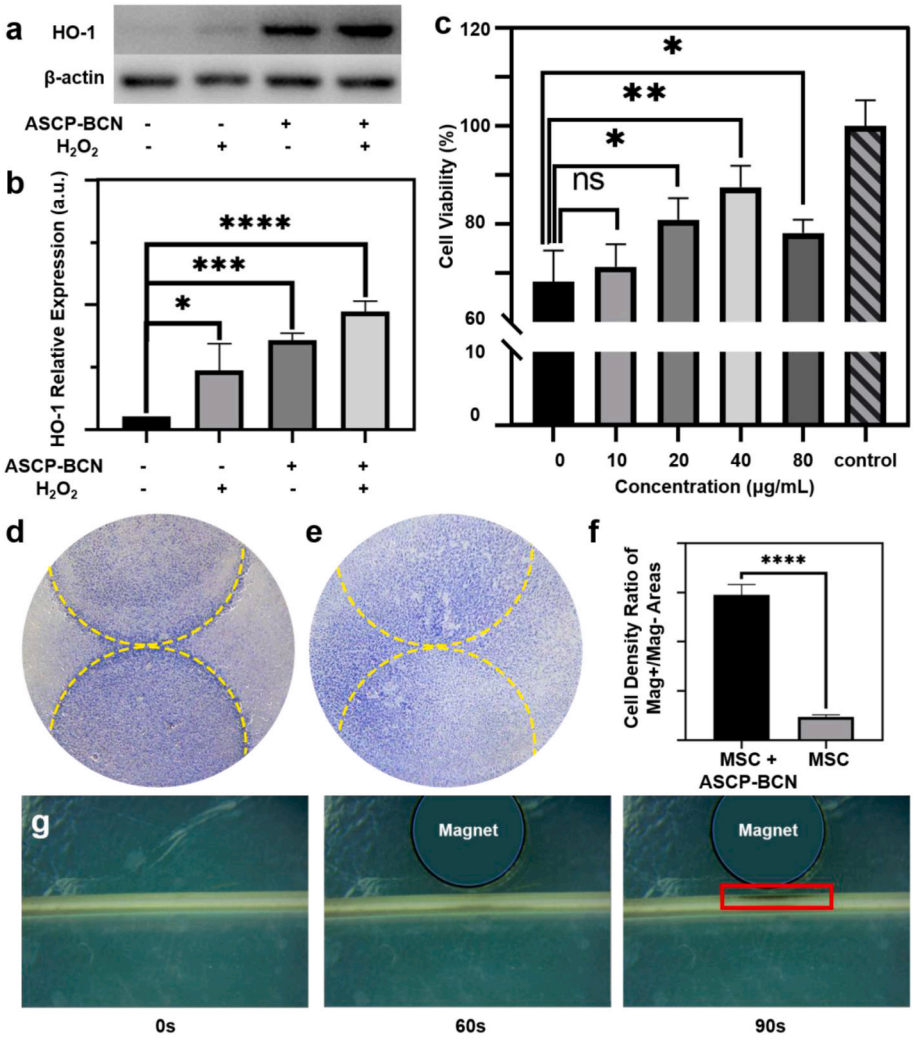

Fig. 4. ASCP-BCN improved MSCs survival as well as endowed them with magnetic-responsiveness *in vitro*. (a) Western blot images and (b) the corresponding expression level of HO-1 of MSCs treated with H_2O_2 alone, 40 μg/mL ASCP-BCNs alone, or 40 μg/mL ASCP-BCNs followed by H_2O_2 (n = 4). (c) Cell viability of ASCP-BCNs labeled MSCs after co-incubation with H_2O_2 evaluated by CCK-8 assay (n = 5). (d, e) The adhesion of (d) ASCP-BCN labeled MSCs and (e) non-treated MSCs was observed by Giemsa staining. The dashed yellow circles indicate the position of magnets on the bottom of the cell culture plates. (f) The cell density ratio of magnetic region to non-magnetic region quantified from (d) and (e). (g) Accumulation of ASCP-BCN labeled MSCs in the tube surrounding the magnet. (*) $p < 0.05$, (**) $p < 0.01$, (***) $p < 0.001$, (****) $p < 0.0001$.

hematological and blood biochemical parameters of ASCP-BCN injected groups did not significantly differ from those of the untreated mice (Fig. S16). Additionally, no notable abnormalities or lesions were observed from the hematoxylin and eosin (H&E) staining of the retrieved organs. Furthermore, the biodistribution of the ASCP-BCN after the transplantation of labeled MSCs was investigated. As shown in Fig. S17, most of the ASCP-BCNs labeling on the MSCs still retained in the lungs with the external magnet field for up to 3 days after transplantation. In contrast, without the magnetic field, most of the injected ASCP-BCN were only retained in the lungs for up to first 3 h, which were then quickly excreted from the body, suggesting that the ASCP-BCN had good metabolism capability and biosafety.

2.7. Monitoring of MSCs by CT imaging

Although the MSC-based therapy has become a potential treatment for PF, tracking transplanted MSCs to elucidate their fate *in vivo* remains a burgeoning challenge [37]. CT imaging is the primary modality for lung tissue imaging due to its high spatial resolution, multi-planar capabilities, fast data acquisition time and reasonable cost, which collectively render it as a promising modality for monitoring MSC fate in the lung [38]. Our *in vitro* results revealed high-intensity CT signal of ASCP-BCN labeled MSCs. To further validate the feasibility of the *in vivo* monitoring of the labeled MSCs *via* CT imaging, MSCs (about 3×10^6 cells per mouse) with or without ASCP-BCN labeling were intratracheally injected into lungs of the mice with BLM-induced PF. Meanwhile, to ascertain the retention of labeled MSCs by an external magnetic field, a magnet was exposed to the chest of the mice for 21 days following injection. An obvious enhanced CT contrast of labeled MSCs was observed in lung tissues post-transplantation compared to the unlabeled MSCs, indicative of the good performance of ASCP-BCN as CT labeling agents (Fig. 5a and Fig. S18). It is noteworthy that the CT signal of labeled MSCs diminished rapidly in the absence of external magnetic field, which may be due to the relocation of the transplanted MSCs towards other organs owning to biological metabolism [8]. Besides, considering that the labeling efficiency of ASCP-BCNs in the MSCs gradually decreased over a longer period of time (Fig. S11), the reduction of CT signal could also be caused by the exocytosis and the metabolism of ASCP-BCN to some extent. In contrast, the CT signal of the labeled MSCs remained clearly visible in magnet group even at the day 7 post-injection, while the CT value of the lung was calculated to be 299 HU, which was 363 HU higher than that of non-magnet group (Fig. 5a and b). Furthermore, the 3D CT images of the lungs at day 1 after transplantation clearly showed the distribution of MSCs, where the labeled MSCs in the lungs of the mouse exposed to the magnet were distinctly higher than that of their counterparts devoid of an external magnet (Fig. 5c). Furthermore, the labeled MSCs could still be observed in the magnet group from the 3D CT images of the lungs at day 14 post-transplantation, while the CT signal of the labeled MSCs could be hardly observed in the absence of the magnet at the same time (Fig. S19). More importantly, the ASCP-BCN could be observed in the lungs of mice with the magnet attachment for up to day 21 post-injection

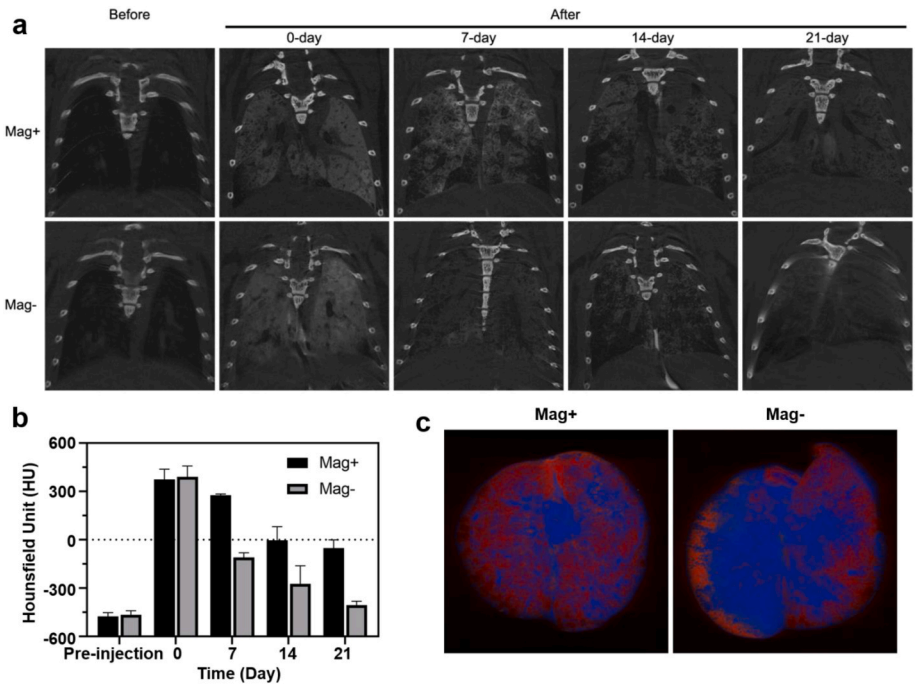

Fig. 5. *In vivo* tracking of ASCP-BCN labeled MSCs *via* CT imaging. (a) CT images and (b) corresponding CT values of lungs before and 0, 7, 14, and 21 days after transplantation of ASCP-BCN labeled MSCs in the presence and absence of magnet attachment. (c) 3D CT images of lungs at day 1 post-injection of ASCP-BCN labeled MSCs in the presence and absence of magnet attachment.

(Fig. S20). These results clearly indicated that the ASCP-BCN labeling of MSCs improved their lung retention by magnetic manipulation.

2.8. Therapeutic effect of MSCs on PF

To assess the feasibility of ASCP-BCN labeled MSCs in the PF treatment, a bleomycin (BLM)-induced PF model in mice was exploited according to the experimental protocol displayed in Fig. 6a. The lung functions of mice significantly reduced due to the BLM treatment, as evidenced by an increase in the breaths per minute, expiratory flow at 50% vital capacity, peak inspiratory flow, and peak expiratory flow (Fig. 6b–e and Fig. S21) [39]. The transplantation of MSCs slightly decreased the aforementioned pulmonary function parameters, which were further alleviated by the transplantation of ASCP-BCN labeled MSCs and magnet attraction, indicating their important role in promoting the therapeutic effect of MSCs. In particular, the respiratory frequency and the peak inspiratory flow of mice in the ASCP-BCN labeled MSCs + magnetic manipulation transplanted group almost reached to that of the control mice. More importantly, the transplantation of labeled MSCs along with magnetic manipulation not only reduced the hydroxyproline (HYP) concentrations in fibrotic lungs, but also decreased the wet to dry ratio of lungs, arising from inflammatory response-mediated pulmonary edema (Fig. 6f and g) [40].

Afterwards, the histopathological damage was assessed to gain further insight into the recovery of PF. As shown in Fig. 6h and Fig. S22, an obvious improvement in the alveolar integrity and orchestration of inflammatory cells could be observed in the treatment groups compared to the PF group. Concomitantly, the lung damage was quantified by Ashcroft score, where the magnetic manipulation group showed a distinct improvement in the treatment efficacy as compared to the mice transplanted with only labeled MSCs (Fig. 6i) [41]. Consistent with the HYP assays, Masson's trichrome staining revealed a reduction in the collagen accumulation in mice transplanted with the labeled MSCs along with magnetic manipulation than that of the BLM group (Fig. 6h, j, and Fig. S22).

Having assessed the improvement in the lung functions and fibrosis status by transplanting labeled MSCs along with the magnetic manipulation, the changes in the expression of fibrotic markers were studied. Firstly, we evaluated the expression of Alpha-smooth muscle actin (α-SMA), which is a marker protein of myofibroblast whose activation mainly contributes to the collagen deposition in fibrosis [42]. As shown in the immunohistochemical staining and the corresponding statistical results, the numbers of α-SMA-positive cells in lungs of PF mice remarkably decreased by the transplantation of labeled MSCs along with magnetic manipulation (Fig. 6h, k). Subsequently, the lung tissues of mice in each group were collected to assess the total expression levels of both α-SMA and transforming growth factor-β (TGF-β), which play a pivotal role in inducing myofibroblasts accumulation [42–44]. In agreement with the immunohistochemistry results, the expression level of total α-SMA was diminished in the treatment group (Fig. 6l, m). More importantly, the expression level of the TGF-β was also significantly inhibited by the transplantation of labeled MSCs and magnetic manipulation (Fig. 6l, m). Taken together, it is found that the retention of the more numbers of viable MSCs in the lungs could lower the expression of TGF-β, thus reducing the myofibroblast accumulation, which may finally alleviate PF and improve lung functions.

In brief, compared to the MSC group, the MSC + ASCP-BCN + magnet group showed significantly improved hydroxyproline content, wet-to-dry ratio and Ashcroft score as well as the proportion of α-SMA positive cells. The existence of significant differences among different groups (Fig. 6f, g, i, k) well confirmed that the cytoprotection and magnetic guidance functions of the ASCP-BCN can improve the therapeutic effect of the MSCs, which further support the notion that most of the ASCP-BCNs can well retain in the MSCs during the treatment, *i.e.*, the main CT signals came from the ASCP-BCN labeled in the MSCs rather than the free ASCP-BCN.

3. Conclusion

In summary, a CoPP aggregation-induced and multifunctional theranostic nanoagent, *i.e.*, ASCP-BCN, was developed for labeling MSCs for PF treatment. ASCP was self-assembled by AuNPs, SPIONs, and

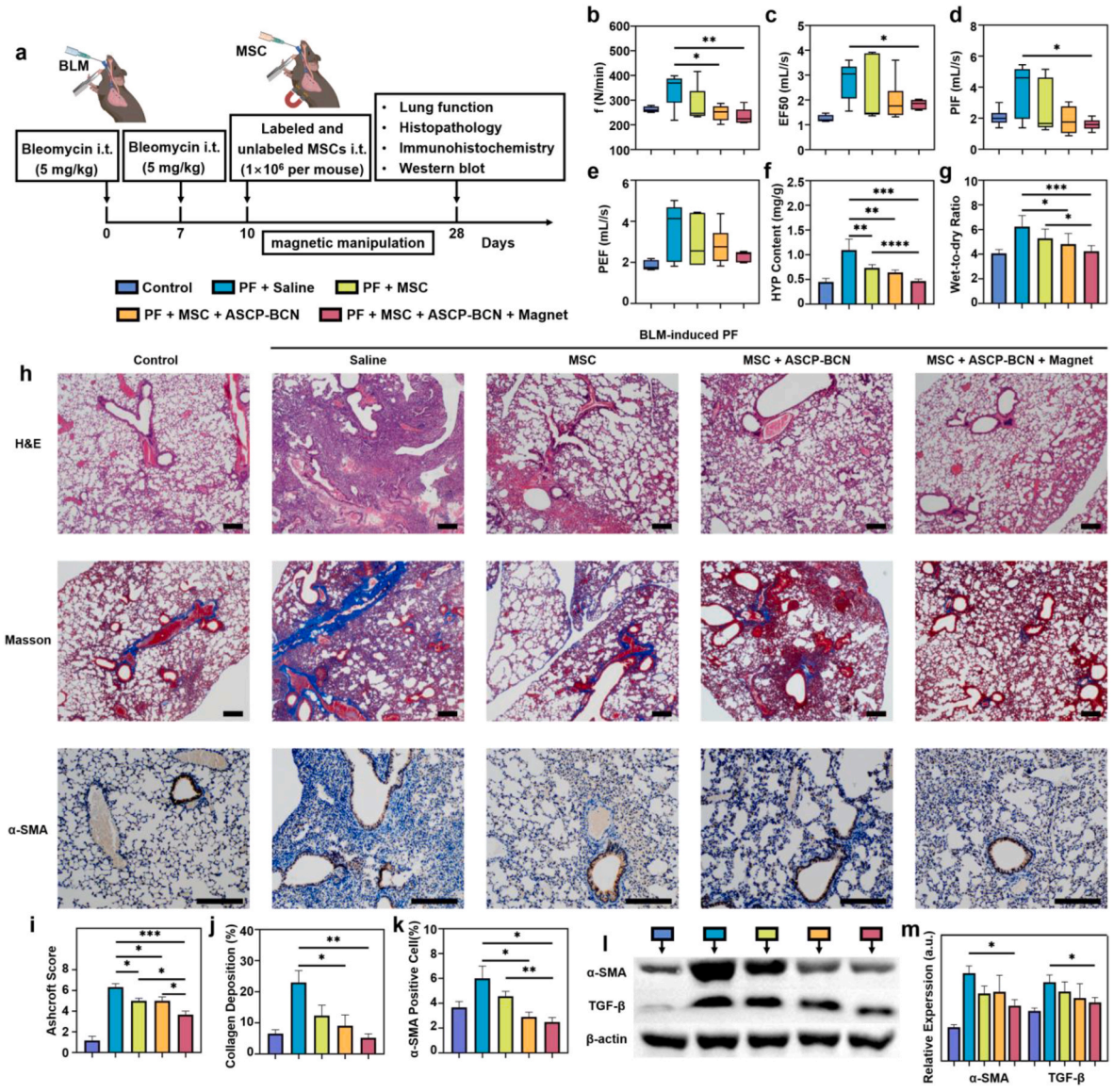

Fig. 6. Therapeutic effects of ASCP-BCN labeled MSCs along with magnetic manipulation on PF. (a) Experimental protocol for MSC therapy of a bleomycin-induced PF mouse model. (b–e) lung functions of mice without treatment (control) and BLM-induced PF model mice with different treatments (Saline, MSCs, ASCP-BCN labeled MSCs, and ASCP-BCN labeled MSCs + magnetic manipulation) at day 28 after the first injection of BLM: (b) breaths per min, (c) expiratory flow at 50% vital capacity, (d) peak inspiratory flow, and (e) peak expiratory flow. (f) content of HYP in lungs. (g) wet-to-dry ratio of lungs in each group. (h) Representative H&E, Masson's trichrome, and α-SMA immunohistochemical staining images of lung slices in each group. Scale bar, 200 μm. (i) Severity of PF evaluated by Ashcroft score corresponding to H&E staining. (j) Area percentage of collagen deposition in lungs measured from Masson's trichrome staining. (k) Percentage of α-SMA positive cells according to the immunohistochemical staining. (l) Western blot analysis of α-SMA and TGF-β in lung tissues and (m) the corresponding relative expression level of α-SMA and TGF-β protein. (*) $p < 0.05$, (**) $p < 0.01$, (***) $p < 0.001$.

CoPP, which respectively served as CT contrast agent, magnetic manipulation agent, and antioxidant drug. Without any additional carriers introduced into the ASCP, high loading efficiency of the functional components could be ensured, thus enabling the reduction of the dose for stem cell labeling. Moreover, the BCN modification on the surface of ASCPs is beneficial to bioorthogonally-label MSCs with a high efficiency. The SPIONs clustered in the ASCP-BCN could significantly increase the retention of transplanted MSCs in lungs *via* an external magnetic field, while the AuNPs may permit for their long-term quantitative monitoring by CT imaging. More importantly, the sustained yet slow release of CoPP from ASCP-BCNs could maintain the intracellular CoPP concentration at an appropriate level to protect MSCs against oxidative stress without an adverse effect on their viability and pluripotency. By intratracheally transplanting ASCP-BCN labeled MSCs into the lungs of mice with a BLM-induced PF and exposing magnets to the chests, the lung functions were found to be significantly improved and the symptoms of PF were alleviated in a TGF-β-mediated signaling pathway. Taken together, this multifunctional theranostic nano-self-assembly with high labeling efficiency, magnetic responsivity, CT recognizability, and cellular protection could present great prospect for stem cell-based therapy for PF.

4. Experimental section

4.1. Chemicals

Oleic acid (OA, technical grade 90%), oleylamine, iron chloride hexahydrate ($FeCl_3{\cdot}6H_2O$), sodium oleate (NaOA), 1-tetradecene (TDE, technical grade 92%), 1-octadecene (ODE, technical grade 90%), tetrachloroaurate ($HAuCl_4$), sodium borohydride ($NaBH_4$), tetraoctylammonium bromide, dodecanethiol, N-hydroxysuccinimide (NHS), 1-

ethyl-3-[3-dimethylaminopropyl]carbodiimide hydrochloride (EDC) and toluene were purchased from Aladdin (Shanghai, China). N-azidoacetylmannosamine-tetraacylated (Ac4ManNAz) was purchased from Sigma Aldrich (Shanghai, China). Dulbecco's modified Eagle's medium (DMEM), fetal bovine serum (FBS), penicillin, and streptomycin were purchased from Gibco (USA). Cobalt protoporphyrin IX (CoPP) was purchased from J&K Scientific (Shanghai, China). Endo BCN-PEG_3-NH_2 was purchased from Click Chemistry Company (Xian, China).

4.2. Characterization

The morphology of materials and cells, as well as the element mapping images were characterized by TEM (JEM-2100F, Jeol, Japan). The surface morphology was assessed by SEM (Magellan 400, FEI Company, Japan). The elemental compositions and concentrations of gold (Au), cobalt (Co), and iron (Fe) were studied by X-ray photoelectron spectroscopy (XPS, ESCALAB 250, Thermo Fisher Scientific, Massachusetts, USA) and inductively-coupled plasma mass spectrometry (ICP-MS; iCAP RQ, Thermo Fisher Scientific, Massachusetts, USA), respectively. The XRD patterns were recorded by a diffractometer (Rigaku D/Max-2550 V). The hydrodynamic sizes and zeta potentials of materials were measured by a Zetasizer Nanoseries (Nano ZS90, United Kingdom). The UV–vis spectra of materials were acquired by using spectrophotometer (Shimadzu UV-3600, Shimadzu Coporation, Kyoto, Japan). The hysteresis loops of materials were obtained by a low temperature magnetic measurement (MPMS XL5, Quantum Design, Calfornia, USA).

4.3. Synthesis of AuNPs

AuNPs (diameter, 5 nm) were prepared by a two-phase reduction method according to a previous report [45]. Firstly, $HAuCl_4$ (30 mM, 10 mL) was mixed with 25 mL of toluene containing 50 mM tetraoctylammonium bromide and stirred until the decolouration of the water phase. Afterwards, dodecanethiol (0.84 mM) was added to the above mixture under stirring. Then, $NaBH_4$ was added dropwise in 15 min and stirred for another 3 h. After decanting the organic phase, ethanol three times to the volume of the solution was added to remove excess thiol. The resultant mixture was kept at −20 °C overnight and the dark brown precipitates were collected through centrifugation followed by resuspension in toluene.

4.4. Synthesis of SPIONs

Oleic acid-modified SPIONs were prepared by a thermal decomposition method following a previous method [46]. Typically, the iron oleate precursor was firstly prepared by stirring NaOA and $FeCl_3{\cdot}6H_2O$ in a mixture solution composed of 8 mL ethanol, 6 mL distilled water, and 14 mL hexane at 70 °C for 6 h under reflux. The resultant iron oleate was separated with separating funnel and purified by rotary evaporator. Then, the 0.45 g of iron oleate was dissolved in a mixture solution composed of 0.88 g TDE, 1.62 g ODE, and 71 mg OA, followed by heating to 290 °C under nitrogen atmosphere for 1 h. The synthesized SPIONs were collected by adding ethanol to demulsify sedimentation and centrifuging at 9000 rotations per minute (rpm) for 10 min. Finally, the SPIONs were resuspended in toluene.

4.5. Preparation of ASCPs and BCN modification

The ASCP was synthesized by an evaporation induced self-assembly method. Briefly, 1 mg of CoPP was dissolved in 50 μL DMSO, and mixed with 1.1 mg AuNPs as well as 1.1 mg SPIONs dispersed in toluene. The mixture was heated at 50 °C for more than 10 min and vortexed for a homogenous mixing. Then the mixture was added to 10 mL of distilled water and sonicated for 5 min at 600 W. After evaporating toluene in a fume hood for 24 h, unreacted CoPP and DMSO were removed by dialysis against distilled water with a dialysis membrane (molecular weight cut off, MWCO, 3500 kDa). Finally, the ASCP was collected by centrifugation at 13,000 rpm for 10 min and washed twice with distilled water.

For surface modification with BCN, 1.2 mg NHS and 0.6 mg EDC were added to 8 mL of 0.15 mg/mL ASCP aqueous solution, followed by 30 min of sonication. Then, 12 μL of 10 mg/mL BCN-PEG_3-NH_2 aqueous solution was added to the mixture and the solution was stirred for 12 h at room temperature. Finally, the ASCP-BCN was collected by centrifugation for 10 min at 13,000 rpm and washed for two times.

4.6. MSC isolation and bioorthogonal labeling

MSCs were isolated from the tibias and femurs of male Sprague-Dawley rats (SLACOM, Shanghai, China, weight, ~200 g) according to a previous report [47]. Briefly, the skeletal muscle was removed from bones by scissors, and the tibias and femurs were flushed with DMEM. The MSCs were collected by centrifugation for 10 min at 1500 rpm and resuspended with high-glucose DMEM containing 10% FBS. The MSCs were cultured in a 10-cm dish (Corning Incorporated, Corning, NY, USA) containing 6 mL culture medium at 37 °C and 5% CO_2 in an incubator (Thermo Scientific, Barrington, IL, USA). The MSCs were purified by replacing culture medium after 48 h to remove non-adherent cells.

For bioorthogonal labeling with ASCP-BCN, MSCs were firstly pretreated with the 10 μM Ac_4ManNAz at 37 °C for 48 h. After washing with PBS twice, MSCs were incubated with ASCP-BCN at 37 °C for 2 h. To observe unlabeled and bioorthogonally labeled MSCs by SEM, MSCs (about 1×10^5 cells per well) were seeded on glass slides placed in a 6-well cell culture plate. After cell adhesion, the MSCs were divided into two groups, one was cultured with complete medium, while the other was bioorthogonally-labeled with 40 μg/mL ASCP-BCN. After labeling, the MSCs were washed by PBS for three times to remove the unlabeled ASCP-BCN and fixed with 4% paraformaldehyde (PFA) for 10 h. The fixed MSCs were dehydrated in graded ethanol series (30, 50, 70, 90, 95, and 100%) and dried, followed by sputter-coating with gold prior to SEM analysis. To obtain high-magnification images of ASCP-BCN labeled MSCs by TEM, the labeled MSCs were fixed with 2.5% glutaraldehyde, and the TEM samples were prepared by resin embedding method. The labeling efficiency of the nanoagent was calculated by measuring the Au content in the MSCs by using inductively coupled plasma optical emission spectrometry (ICP-OES). To determine SPION content in the labeled MSCs, they were seeded on glass slides placed in a 6-well cell culture plate (about 1×10^5 cells per well), and divided into four groups, including Ac_4ManNAz, ASCP-BCN, Ac_4ManNAz/ASCP, and Ac_4ManNAz/ASCP-BCN. After washing three times with PBS, the MSCs were stained with a Perls staining kit and observed with a light microscope.

4.7. In vitro evaluation of CT imaging capacity of ASCP-BCN

To evaluate the CT imaging capability of ASCP-BCN, aqueous solutions of ASCP-BCN with different Au concentrations (0, 125, 250, 500, and 1000 μg/mL) were prepared. The liquid samples were loaded in removable 96-well plates. The CT images were obtained by a micro-CT scanner (BRUKER SKYSCAN) and quantitatively analyzed by CTAN (BRUKER) software. The HU values were calculated by using linear extrapolation as follows;

$$HU = 1000 \times \frac{\mu_x - \mu_{water}}{\mu_{water} - \mu_{air}}$$

where μ_x, μ_{water}, and μ_{air} indicate the attenuation coefficients of the liquid sample, distilled water and air recorded from the CT measurement.

To evaluate the CT signal of labeled MSCs, ASCP-BCNs at different concentrations (0, 10, 20, and 40 μg/mL) were used to label MSCs. After collecting MSCs by trypsinization, 5×10^5 labeled MSCs of each group,

as well as different amounts (0, 2.5×10^5, 5×10^5, and 1×10^6) of MSCs labeled by 40 μg/mL ASCP-BCN were separately dispersed in 100 μL PBS and loaded in removable 96-well plates. Then, the CT phantom images were acquired by the micro-CT scanner.

4.8. In vitro evaluations of cytotoxicity and antioxidant stress capacity of ASCP-BCN

To assess the cytotoxicity of ASCP-BCN, MSCs were seeded in 96-well culture plates at a density of 1×10^4 per well and cultured in an incubator with 10 μM Ac_4ManNAz for 48 h. Then, various concentrations of ASCP-BCN were used to treat MSCs for 6 h. The labeled MSCs were washed with sterile PBS twice, and the medium was changed every three days. The viability of MSCs was examined by using cell counting kit 8 (CCK-8) 1, 7, and 14 days after labeling.

To evaluate the antioxidant capacity of ASCP-BCN, MSCs were labeled with ASCP-BCN at different concentrations (0, 10, 20, and 40 μg/mL) in a 96-well plate and treated with low-glucose DMEM containing 100 μM H_2O_2 for 24 h. MSCs were then washed with PBS three times, and the cell viability was evaluated with a standard CCK-8 assay. Furthermore, to evaluate its inhibition capacity of cell apoptosis, MSCs were bioorthogonally labeled with ASCP-BCN at 40 μg/mL in a 96-well plate and treated with low-glucose DMEM containing 100 μM H_2O_2 for 12 h. The cell apoptosis was assessed by a calcein-AM/PI staining kit.

4.9. Osteogenic and adipogenic differentiation evaluations in vitro

Osteogenic induction differentiation complete medium was prepared by adding 100 nM dexamethasone, 10 mM glycerophosphate disodium salt hydrate, and 50 μM 2-phospho-L-ascorbic acid trisodium salt into the high-glucose DMEM containing 10% FBS. Adipogenic induction differentiation complete medium was prepared by adding 1 μM dexamethasone, 10 μg/mL insulin, 200 μM indomethacin, and 500 μM 3-isobutyl-1-methylxanthine to the high-glucose DMEM containing 10% FBS.

MSCs were seeded into 96-well plates at a density of 1×10^4 per well, and cultured for 12 h, followed by treatments with the either Ac_4ManNAz glycolengineering alone or bioorthogonal labeling with ASCP-BCN at 40 or 80 μg/mL. The cells without any treatment were used as controls. The medium was then replaced by osteogenic or adipogenic differentiation medium. The medium was replaced by fresh induction differentiation medium every three days, and the MSCs were further cultured for 14 days. After fixing the MSCs by 4% PFA for 10 min, MSCs induced into osteogenic differentiation or adipogenic differentiation were stained with alizarin red S for 5 min or oil red O for 20 min, respectively. Then, the MSCs were washed with PBS, and the calcified nodules and lipid droplets in MSCs were observed under a light microscope. The quantitative results of osteogenic differentiation were obtained by dissolving the dye in MSCs with 10% cetylpyridinium chloride and measuring the absorbance at 562 nm wavelength by a microplate analyzer. Similarly, the quantitative results of adipogenic differentiation were determined by dissolving the lipid droplets with isopropanol and measuring the absorbance at 450 nm by a microplate analyzer.

4.10. Wounding healing assay

The effect of ASCP-BCN labeling on the chemotaxis of MSCs was evaluated by a wound healing assay. Briefly, MSCs were seeded in a 6-well cell culture plate (about 1×10^5 cells per well), and divided into two groups: (a) control and (b) bioorthogonal labeling with 40 μg/mL ASCP-BCN. Three parallel scratches were made in each well with the tip of a 100 μL pipette. The migration condition was observed by a fluorescence microscope immediately as well as after 12 h and 24 h, and the cell migration rate was measured using ImageJ software.

4.11. Magnetic responsivity

The unlabeled MSCs and ASCP-BCN labeled MSCs were seeded in a 24-well culture plate with a pair of NdFeB magnets (Grade N35, diameter 10 mm, height 2 mm) attached to the bottom of the plate. After 12 h, MSCs were washed by PBS twice and fixed with 4% PFA for 10 min, followed by Giemsa staining. The adhesive MSCs were observed with a light microscope and the quantitative result was calculated by ImageJ software.

To mimic the environment of transplanted MSCs *in vivo*, the ASCP-BCN labeled MSCs were dispersed in PBS at the concentration of 1×10^6 cells/mL and injected into a plastic cylinder at a flow rate of 0.2 mL/min by using a microinjection bump. A NdFeB magnet was put close to the tube 1 min after injection, and the suspension flow was recorded with a light microscope.

4.12. Western blotting

The expression levels of HO-1 in MSCs and specific proteins in lung tissues were tested by western blotting. Briefly, the total protein was obtained by lysing MSCs or lung tissues. After quantifying the protein concentration by BCA kit, the same amount of protein in each sample was separated through SDS-PAGE gel electrophoresis, and transferred to a PVDF membrane. The nonspecific proteins were sealed up by TBST buffer containing 5% skimmed milk powder, followed by incubating the specific primary antibodies (β-actin, HO-1, α-SMA, or TGF-β) at 4 °C overnight. Then, the membrane was washed with TBST buffer and incubated with secondary antibodies (1:5000) at room temperature for 1 h. The protein content was assessed by chemiluminescence.

4.13. Bleomycin-induced pulmonary fibrosis model and MSC transplantation

All animal procedures were performed with the approval of the Shanghai General Hospital Clinical Center Laboratory Animal Welfare & Ethics Committee (Protocol No.2021AWS0123). 36 male C57BL/6 mice were acclimated for up to 1 week and divided randomly into six groups: (1) Control, (2) PF, (3) PF + saline, (4) PF + MSC, (5) PF + ASCP-BCN labeled MSC, and (6) PF + ASCP-BCN labeled MSC + magnet (n = 6). The PF was induced by bleomycin (BLM). Briefly, the mice were anesthetized and BLM (5 mg/kg) dispersed in 100 μL sterile saline was slowly administrated into the tracheal lumen through an endotracheal intubation. Mice in saline group received only 100 μL sterile saline. The above procedure was repeated at the 7th day after administration. The unlabeled MSCs and labeled MSCs (1×10^6 cells per mouse) in 100 μL saline were intratracheally transplanted into the lungs of mice at the 10th day after the first injection of BLM. A NdFeB magnet was attached to the chest of each mouse in PF + ASCP-BCN labeled MSC + magnet group. Mice were sacrificed at day 28 after the first injection of BLM to harvest pulmonary tissues. The degree of pulmonary fibrosis is assessed by hematoxylin and eosin (H&E) and Masson's trichrome staining.

4.14. Biodistribution

ASCP-BCN labeled MSCs were intratracheally transplanted into the lungs of mice (1×10^6 cells per mouse). A NdFeB magnet was attached to the chest of each mouse in PF + ASCP-BCN labeled MSC + magnet group. Mice were sacrificed and their main organs (hearts, livers, spleens, lungs, and kidneys) were isolated at different time points (3 h, 1 d, and 3 d after MSC transplantation). Then the obtained organs were digested for the measurement of Au element by ICP-OES.

4.15. In vivo CT scanning

In order to clearly observe the transplanted MSCs in the lungs through CT imaging, unlabeled MSCs and ASCP-BCN labeled MSCs (3 ×

10^6 cells per mouse) in 100 μL saline were intratracheally injected into the lungs of mice. A magnet (Grade N35, diameter 15 mm, height 2 mm) was exposed to the chest of the mice in magnet group for 21 days after injection. *In vivo* CT scanning of the lungs was performed before injection and at 0 h, 1 d, 7 d, 14 d, and 21 d after injection. CT images were quantitatively analyzed by CTAN (Bruker, Massachusetts, USA) software, and the regions of interest (ROIs) with the same area were drawn over the area of the labeled MSCs within the lung of each mouse. The average HU values were calculated from these ROIs in slices (n = 3).

4.16. Evaluation of lung function

Mice were weighed at day 28 after the first injection of BLM, and their lung function data was recorded by putting them into a WBP respiratory whole-body plethysmography. The mouse lungs were then harvested for further characterizations. One lobe of lung in each mouse was taken out and the blood on the surface was gently wiped off. The lung tissues were weighed and baked at 60 °C for 72 h. The dry lung tissues were weighed again and the wet-to-dry ratio of lung was obtained. The HYP concentrations in lung tissues were assessed with a HYP assay kit.

4.17. Histopathology and immunohistochemistry analysis

The mouse lungs were embedded in paraffin, sectioned and subjected to H&E or Masson's trichrome staining. The Ashcroft score was rated and the area of collagen deposition was counted by ImageJ software to quantitatively assess the degree of fibrosis. The range of pathological scoring in Ashcroft score was 0 (normal lung) to 8 (total fibrous obliteration).

For immunohistochemistry analysis, the lung sections were fixed with 4% PFA and the endogenous catalase was removed with methanol containing 3% hydrogen peroxide, followed by recovering the antigen through heating in a pressure cooker with citric acid buffer. The lung tissues were incubated with sheep serum to block the nonspecific sites before incubating with the primary antibody of α-SMA (Abcam) and secondary antibody successively. The stained lung slides were observed with a light microscope.

CRediT authorship contribution statement

Yimeng Shu: Conceptualization, Investigation, Writing – original draft. **Ming Ma:** Conceptualization, Funding acquisition, Writing – review & editing. **Xiaoxia Pan:** Software, Resources. **Muhammad Shafiq:** Writing – review & editing. **Huizhu Yu:** Investigation, Resources. **Hangrong Chen:** Supervision, Funding acquisition, Writing – review & editing.

Declaration of competing interest

The authors declare that they have no known competing financial interests or personal relationships that could have appeared to influence the work reported in this paper.

Acknowledgements

This work was supported by the National Natural Science Foundation of China (Grant Nos.52072392, 32030061, 82171951), the Key Program for Basic Research of Shanghai (Grant Nos.20JC1411900, 21JC1406000), Shanghai Rising-Star Program (Grant No.19QA1410300), and Youth Innovation Promotion Association CAS (Grant No.2020255). We would like to thank Dr. Minghua Yao from the Shanghai General Hospital for supporting *in vivo* experiment.

Appendix A. Supplementary data

Supplementary data to this article can be found online at https://doi.org/10.1016/j.bioactmat.2022.08.008.

References

[1] F.J. Martinez, H.R. Collard, A. Pardo, G. Raghu, L. Richeldi, M. Selman, J. J. Swigris, H. Taniguchi, A.U. Wells, Idiopathic pulmonary fibrosis, Nat. Rev. Dis. Prim. 3 (2017), 17074.
[2] H.J. Kim, D. Perlman, R. Tomic, Natural history of idiopathic pulmonary fibrosis, Respir. Med. 109 (6) (2015) 661–670.
[3] A. Tzouvelekis, R. Toonkel, T. Karampitsakos, K. Medapalli, I. Ninou, V. Aidinis, D. Bouros, M.K. Glassberg, Mesenchymal stem cells for the treatment of idiopathic pulmonary fibrosis, Front. Med. 5 (142) (2018).
[4] B. Alvarez-Palomo, L.I. Sanchez-Lopez, Y. Moodley, M.J. Edel, A. Serrano-Mollar, Induced pluripotent stem cell-derived lung alveolar epithelial type II cells reduce damage in bleomycin-induced lung fibrosis, Stem Cell Res. Ther. 11 (1) (2020) 213.
[5] S. Yang, P. Liu, Y. Jiang, Z. Wang, H. Dai, C. Wang, Therapeutic applications of mesenchymal stem cells in idiopathic pulmonary fibrosis, Front. Cell Dev. Biol. 9 (2021), 639657.
[6] J.G. Wilson, K.D. Liu, H. Zhuo, L. Caballero, M. McMillan, X. Fang, K. Cosgrove, R. Vojnik, C.S. Calfee, J.-W. Lee, A.J. Rogers, J. Levitt, J. Wiener-Kronish, E. K. Bajwa, A. Leavitt, D. McKenna, B.T. Thompson, M.A. Matthay, Mesenchymal stem (stromal) cells for treatment of ARDS: a phase 1 clinical trial, Lancet Respir. Med. 3 (1) (2015) 24–32.
[7] B. Thangakunam, D.J. Christopher, Allogeneic human mesenchymal stem cells in patients with idiopathic pulmonary fibrosis: well done, but subsequent doses may Be vital, Chest 153 (1) (2018) 287.
[8] E. Eggenhofer, V. Benseler, A. Kroemer, F.C. Popp, E.K. Geissler, H.J. Schlitt, C. C. Baan, M.H. Dahlke, M.J. Hoogduijn, Mesenchymal stem cells are short-lived and do not migrate beyond the lungs after intravenous infusion, Front. Immunol. 3 (2012) 297.
[9] A. Vasconcelos-dos-Santos, P.H. Rosado-de-Castro, S.A. Lopes de Souza, J. da Costa Silva, A.B. Ramos, G. Rodriguez de Freitas, L.M. Barbosa da Fonseca, B. Gutfilen, R. Mendez-Otero, Intravenous and intra-arterial administration of bone marrow mononuclear cells after focal cerebral ischemia: is there a difference in biodistribution and efficacy? Stem Cell Res. 9 (1) (2012) 1–8.
[10] C.R. Kliment, T.D. Oury, Oxidative stress, extracellular matrix targets, and idiopathic pulmonary fibrosis, Free Radic. Biol. Med. 49 (5) (2010) 707–717.
[11] L.H.A. Silva, M.A. Antunes, C.C. Dos Santos, D.J. Weiss, F.F. Cruz, P.R.M. Rocco, Strategies to improve the therapeutic effects of mesenchymal stromal cells in respiratory diseases, Stem Cell Res. Ther. 9 (1) (2018) 45.
[12] Y. Fu, D.L. Kraitchman, Stem cell labeling for noninvasive delivery and tracking in cardiovascular regenerative therapy, Expert Rev. Cardiovasc. Ther. 8 (8) (2010) 1149–1160.
[13] M. Ma, Y. Shu, Y. Tang, H. Chen, Multifaceted application of nanoparticle-based labeling strategies for stem cell therapy, Nano Today 34 (2020).
[14] H. Bao, Y. Xia, C. Yu, X. Ning, X. Liu, H. Fu, Z. Chen, J. Huang, Z. Zhang, CT/Bioluminescence dual-modal imaging tracking of mesenchymal stem cells in pulmonary fibrosis, Small 15 (46) (2019), e1904314.
[15] P.J. Kempen, S. Greasley, K.A. Parker, J.L. Campbell, H.Y. Chang, J.R. Jones, R. Sinclair, S.S. Gambhir, J.V. Jokerst, Theranostic mesoporous silica nanoparticles biodegrade after pro-survival drug delivery and ultrasound/magnetic resonance imaging of stem cells, Theranostics 5 (6) (2015) 631–642.
[16] F. Chen, E.R. Zhao, G. Hableel, T. Hu, T. Kim, J. Li, N.I. Gonzalez-Pech, D.J. Cheng, J.E. Lemaster, Y. Xie, V.H. Grassian, G.L. Sen, J.V. Jokerst, Increasing the efficacy of stem cell therapy via triple-function inorganic nanoparticles, ACS Nano 13 (6) (2019) 6605–6617.
[17] L. Lu, Y. Wang, F. Zhang, M. Chen, B. Lin, X. Duan, M. Cao, C. Zheng, J. Mao, X. Shuai, J. Shen, MRI-visible siRNA nanomedicine directing neuronal differentiation of neural stem cells in stroke, Adv. Funct. Mater. 28 (14) (2018), 1706769.
[18] S. Qi, P. Zhang, M. Ma, M. Yao, J. Wu, E. Makila, J. Salonen, H. Ruskoaho, Y. Xu, H. A. Santos, H. Zhang, Cellular internalization-induced aggregation of porous silicon nanoparticles for ultrasound imaging and protein-mediated protection of stem cells, Small 15 (1) (2019), e1804332.
[19] D. Huang, Y. Cao, X. Yang, Y. Liu, Y. Zhang, C. Li, G. Chen, Q. Wang, A nanoformulation-mediated multifunctional stem cell therapy with improved beta-amyloid clearance and neural regeneration for alzheimer's disease, Adv. Mater. 33 (13) (2021), 2006357.
[20] J.G. Croissant, K.S. Butler, J.I. Zink, C.J. Brinker, Synthetic amorphous silica nanoparticles: toxicity, biomedical and environmental implications, Nat. Rev. Mater. 5 (12) (2020) 886–909.
[21] S. Shao, V. Rajendiran, J.F. Lovell, Metalloporphyrin nanoparticles: coordinating diverse theranostic functions, Coord. Chem. Rev. 379 (2019) 99–120.
[22] P. Huang, X. Qian, Y. Chen, L. Yu, H. Lin, L. Wang, Y. Zhu, J. Shi, Metalloporphyrin-Encapsulated biodegradable nanosystems for highly efficient magnetic resonance imaging-guided sonodynamic cancer therapy, J. Am. Chem. Soc. 139 (3) (2017) 1275–1284.
[23] J. Li, Y. Guo, X. Duan, B. Li, Heme oxygenase-1 (HO-1) assists inorganic arsenic-induced immune tolerance in murine dendritic cells, Chemosphere 264 (Pt 2) (2021), 128452.

[24] M. Yao, X. Shi, C. Zuo, M. Ma, L. Zhang, H. Zhang, X. Li, G.Y. Yang, Y. Tang, R. Wu, Engineering of SPECT/photoacoustic imaging/antioxidative stress triple-function nanoprobe for advanced mesenchymal stem cell therapy of cerebral ischemia, ACS Appl. Mater. Inter. 12 (34) (2020) 37885–37895.
[25] Y. Shan, J. Pepe, T.H. Lu, K.K. Elbirt, R.W. Lambrecht, H.L. Bonkovsky, Induction of the heme oxygenase-1 gene by metalloporphyrins, Arch. Biochem. Biophys. 380 (2) (2000) 219–227.
[26] Role of Bach1 and Nrf2 in up-regulation of the heme oxygenase-1 gene by cobalt protoporphyrin, Faseb. J. 20 (14) (2006) 2651–2653.
[27] L.-P. Zhao, R.-R. Zheng, H.-Q. Chen, L.-S. Liu, X.-Y. Zhao, H.-H. Liu, X.-Z. Qiu, X.-Y. Yu, H. Cheng, S.-Y. Li, Self-delivery nanomedicine for O2-economized photodynamic tumor therapy, Nano Lett. 20 (3) (2020) 2062–2071.
[28] Y. Duan, D. Hu, B. Guo, Q. Shi, M. Wu, S. Xu, Kenry, X. Liu, J. Jiang, Z. Sheng, H. Zheng, B. Liu, Nanostructural control enables optimized photoacoustic–fluorescence–magnetic resonance multimodal imaging and photothermal therapy of brain tumor, Adv. Funct. Mater. 30 (1) (2019).
[29] A. Walther, A.H.E. Müller, Janus particles: synthesis, self-assembly, physical properties, and applications, Chem. Rev. 113 (7) (2013) 5194–5261.
[30] M.C. Biesinger, B.P. Payne, A.P. Grosvenor, L.W.M. Lau, A.R. Gerson, R.S.C. Smart, Resolving surface chemical states in XPS analysis of first row transition metals, oxides and hydroxides: Cr, Mn, Fe, Co and Ni, Appl. Surf. Sci. 257 (7) (2011) 2717–2730.
[31] Y. Li, G. Liu, J. Ma, J. Lin, H. Lin, G. Su, D. Chen, S. Ye, X. Chen, X. Zhu, Z. Hou, Chemotherapeutic drug-photothermal agent co-self-assembling nanoparticles for near-infrared fluorescence and photoacoustic dual-modal imaging-guided chemo-photothermal synergistic therapy, J. Control. Release 258 (2017) 95–107.
[32] Y. Liu, J.R. Ashton, E.J. Moding, H. Yuan, J.K. Register, A.M. Fales, J. Choi, M. J. Whitley, X. Zhao, Y. Qi, Y. Ma, G. Vaidyanathan, M.R. Zalutsky, D.G. Kirsch, C. T. Badea, T. Vo-Dinh, A plasmonic gold nanostar theranostic probe for in vivo tumor imaging and photothermal therapy, Theranostics 5 (9) (2015) 946–960.
[33] D. Yu, M. Ma, Z. Liu, Z. Pi, X. Du, J. Ren, X. Qu, MOF-encapsulated nanozyme enhanced siRNA combo: control neural stem cell differentiation and ameliorate cognitive impairments in Alzheimer's disease model, Biomaterials 255 (2020), 120160.
[34] X. Ning, H. Bao, X. Liu, H. Fu, W. Wang, J. Huang, Z. Zhang, Long-term in vivo CT tracking of mesenchymal stem cells labeled with Au@BSA@PLL nanotracers, Nanoscale 11 (43) (2019) 20932–20941.
[35] M. Yao, M. Ma, H. Zhang, Y. Zhang, G. Wan, J. Shen, H. Chen, R. Wu, Mesopore-induced aggregation of cobalt protoporphyrin for photoacoustic imaging and antioxidant protection of stem cells, Adv. Funct. Mater. 28 (47) (2018).
[36] M. Yu, L. Chen, Z. Peng, D. Wang, Y. Song, H. Wang, P. Yao, H. Yan, A.K. Nüssler, L. Liu, W. Yang, Embryotoxicity caused by DON-induced oxidative stress mediated by Nrf2/HO-1 pathway, Toxins 9 (6) (2017) 188.
[37] F.A. Oliveira, M.P. Nucci, I.S. Filgueiras, J.M. Ferreira, L.P. Nucci, J.B. Mamani, F. Alvieri, L.E.B. Souza, G.N.A. Rego, A.T. Kondo, N. Hamerschlak, L.F. Gamarra, Noninvasive tracking of hematopoietic stem cells in a bone marrow transplant model, Cells 9 (4) (2020).
[38] E. Hammond, J.D. Newell Jr., S.K. Dilger, N. Stoyles, J. Morgan, J.P. Sieren, D. R. Thedens, E.A. Hoffman, D.K. Meyerholz, J.C. Sieren, Computed tomography and magnetic resonance imaging for longitudinal characterization of lung structure changes in a yucatan miniature pig silicosis model, Toxicol. Pathol. 44 (3) (2016) 373–381.
[39] S.D. Lok, D.W. Cockcroft, A. Simidchiev, Assessment of ratio of peak expiratory flow rate to vital capacity for identifying pulmonary fibrosis, Clin. Invest. Med. 44 (1) (2021) E25–E27.
[40] Y. Zhao, X. Lan, Y. Wang, X. Xu, S. Lu, X. Li, B. Zhang, G. Shi, X. Gu, C. Du, H. Wang, Human endometrial regenerative cells attenuate bleomycin-induced pulmonary fibrosis in mice, Stem Cell. Int. 2018 (2018), 3475137.
[41] T. Ashcroft, J.M. Simpson, V. Timbrell, Simple method of estimating severity of pulmonary fibrosis on a numerical scale, J. Clin. Pathol. 41 (4) (1988) 467.
[42] H. Kang, Role of MicroRNAs in TGF-β signaling pathway-mediated pulmonary fibrosis, Int. J. Mol. Sci. 18 (12) (2017).
[43] N.C. Henderson, F. Rieder, T.A. Wynn, Fibrosis: from mechanisms to medicines, Nature 587 (7835) (2020) 555–566.
[44] T.-H. Lee, C.-F. Yeh, Y.-T. Lee, Y.-C. Shih, Y.-T. Chen, C.-T. Hung, M.-Y. You, P.-C. Wu, T.-P. Shentu, R.-T. Huang, Y.-S. Lin, Y.-F. Wu, S.-J. Lin, F.-L. Lu, P.-N. Tsao, T.-H. Lin, S.-C. Lo, Y.-S. Tseng, W.-L. Wu, C.-N. Chen, C.-C. Wu, S.-L. Lin, A. I. Sperling, R.D. Guzy, Y. Fang, K.-C. Yang, Fibroblast-enriched endoplasmic reticulum protein TXNDC5 promotes pulmonary fibrosis by augmenting TGFβ signaling through TGFBR1 stabilization, Nat. Commun. 11 (1) (2020) 4254.
[45] A. Al Zaki, D. Joh, Z. Cheng, A.L. De Barros, G. Kao, J. Dorsey, A. Tsourkas, Gold-loaded polymeric micelles for computed tomography-guided radiation therapy treatment and radiosensitization, ACS Nano 8 (1) (2014) 104–112.
[46] F. Yang, A. Skripka, M.S. Tabatabaei, S.H. Hong, F. Ren, Y. Huang, J.K. Oh, S. Martel, X. Liu, F. Vetrone, D. Ma, Magnetic photoluminescent nanoplatform built from large-pore mesoporous silica, Chem. Mater. 31 (9) (2019) 3201–3210.
[47] I.M. Barbash, P. Chouraqui, J. Baron, M.S. Feinberg, S. Etzion, A. Tessone, L. Miller, E. Guetta, D. Zipori, L.H. Kedes, R.A. Kloner, J. Leor, Systemic delivery of bone marrow-derived mesenchymal stem cells to the infarcted myocardium: feasibility, cell migration, and body distribution, Circulation 108 (7) (2003) 863–868.